Multifunctional Leaf-Vein Micro-Channel Spar Architecture for Cryogenic Hydrogen Thermal Management and Structural Load-Bearing in Long-Endurance UAVs

Majd Chalak*

Independent Researcher

San Mateo, CA, USA

ABSTRACT

Long-endurance hydrogen PEM fuel-cell UAVs must pre-heat cryogenic hydrogen from $-150\,^{\circ}\mathrm{C}$ to 70–85 °C at the fuel cell inlet while simultaneously dissipating kilowatts of motor and stack waste heat. Conventional approaches require separate dedicated subsystems, imposing mass penalties that reduce endurance.

This paper presents a *conceptual design* for a *leaf-vein micro-channel spar architecture* in which the primary wing spars of the MARID UAV simultaneously carry structural bending and torsion loads and serve as cryogenic hydrogen thermal conduits. A hierarchical three-level channel network distributes flow through 160 terminal micro-channels ($D_i = 1.5\,\mathrm{mm}$) across the wing and tail surfaces, eliminating dedicated pre-heating and waste-heat rejection hardware while routing cold hydrogen through thermally critical zones to suppress the vehicle's infrared (IR) signature—a key requirement for covert ISR missions.

A one-dimensional finite-segment thermal model demonstrates that ambient spar pre-heating is significant but insufficient at all altitudes. An electric trim heater—1,220 W at sea level (47% of total electrical demand) to 1,650 W at the tropopause—closes the energy balance, bringing the outlet temperature to 77.3 °C within the required 70–85 °C PEM operating window. The 23:1 recirculation pump power is negligible (0.0015 W), and GH_2's specific heat ($\approx$13,500 $\mathrm{J\,kg^{-1}K^{-1}}$) makes it uniquely suited to this combined thermal-management and propulsion role.

. INTRODUCTION

A. Motivation

Hydrogen PEM fuel cells offer energy densities an order of magnitude higher than lithium-ion batteries at the system level, making them the enabling technology for UAV endurance missions exceeding 24 hours [1]. However, PEM stacks operate optimally between 60 and 85 °C; membrane degradation accelerates outside this window [2]. Cryogenic hydrogen storage—whether compressed gaseous (GH_2, $-150\,^{\circ}\mathrm{C}$ at 350 bar) or liquid (LH_2, $-253\,^{\circ}\mathrm{C}$)— therefore requires a pre-heating system before the fuel cell inlet.

Simultaneously, electric motors, the PEM stack, and avionics collectively dissipate several kilowatts of waste heat. On a long-endurance ISR platform, this heat must be managed to prevent structural overtemperature and, critically, to suppress the vehicle's infrared plume. Conventional designs route separate cooling loops through heat exchangers and radiators, adding significant dry mass [3].

B. Proposed Approach

This paper proposes eliminating both the pre-heater and the cooling subsystem by routing cryogenic hydrogen directly through the wing spars. The spars simultaneously carry aerodynamic bending and torsion loads and act as distributed heat exchangers. As cold H_2 flows from the cryogenic storage vessel outboard through the wing, it absorbs waste heat deposited at motor mounts and the PEM bay, arriving at the fuel cell inlet pre-heated to the required temperature. No dedicated heat exchangers, radiators, or separate cooling loops are required.

The architecture is inspired by biological leaf-vein networks, in which a hierarchical branching structure simultaneously provides mechanical support and fluid transport—a well-established example of structural multifunctionality in nature [4].

C. Related Work

Multifunctional structures that combine load-bearing and fluid transport functions have been explored for satellite thermal control [5] and battery thermal management in electric vehicles [6]. Micro-channel heat exchangers embedded in composite panels have been demonstrated for airborne electronics cooling [7]. However, the application of this concept to cryogenic hydrogen pre-heating within a primary structural spar—where the working fluid is also the fuel—has not been previously reported.

D. Paper Contributions

This paper makes the following contributions:

1. A novel dual-function wing spar architecture that eliminates dedicated H_2 pre-heating and waste heat rejection subsystems.

2. A one-dimensional finite-segment thermal model validated against the 70–85 °C PEM inlet requirement for the MARID 113.6 kg UAV.

3. Quantification of the recirculation pump requirement (23:1 thermal-to-fuel flow ratio for internal heat only) and its negligible impact on endurance.

4. A working fluid trade study demonstrating GH_2's suitability relative to thermal oil and water.

5. Analysis of the IR signature suppression mechanism enabled by selective cold-hydrogen routing.

. MARID PLATFORM

A. Vehicle Overview

The MARID (Multi-Axis Rotary-wing Integrated Drone) is a fixed-wing UAV with independently rotating main wings and V-tail surfaces that provide full pitch, roll, and yaw authority without conventional control surfaces [12]. Key geometric and mass properties, extracted from the ROS2/Gazebo simulation model, are summarized in Table 1.

Table 1: MARID vehicle properties (from simulation URDF); mass is a provisional structural baseline only—see note below

Parameter	Value	Source
Structural mass (URDF)†	113.6 kg	Link mass summation
Fuselage length	3.0 m	Tail joint at $x = -2.56$ m
Wing semispan (joint to tip)	1.5 m	Inertial CoM at $y = 0.61$ m
Wing root offset from CL	0.50 m	Wing joint y-position
Wing mass (each)	3.662 kg	URDF inertial
Thruster configuration	1 (single)	Top-mounted aft-fuselage pusher
Wing rotation limit	$\pm 8.6°$	Joint limits ± 0.15 rad
Design endurance	$>$48 hr	Design objective
Design mission	Covert ISR	—

† The URDF mass of 113.6 kg represents the structural airframe as modeled in simulation only. It excludes: the single high-power thruster system (motor + propeller + ESC, estimated 7–16 kg); cryogenic hydrogen storage and tank (fuel + LH_2 tank: estimated 43–53 kg); startup and contingency battery pack (960 Wh at 1.30× safety, estimated 3.8–4.8 kg); PEM fuel cell stack; and sensor payload. Accounting for these, real MTOW is estimated at **175–210 kg**. All thermal analyses in this paper scale proportionally with gross mass and remain architecturally valid at the corrected MTOW.

B. Propulsion and Energy System

The primary energy source is a PEM hydrogen fuel cell stack supplemented by a lithium battery buffer that serves two roles: (i) transient peak power during takeoff and manoeuvres, and (ii) sole electrical supply during cold-start, before the fuel cell reaches operating temperature. Hydrogen is stored cryogenically and fed to the fuel cell after passing through the micro-channel spar system described in Section 3.

Battery Sizing

At cold-start the trim heater (Section 3.5) must pre-heat the H_2 supply before the PEM stack can sustain output. The battery must therefore cover two sequential energy demands:

1. **Trim heater phase** (PEM offline, ≈10 min): worst-case heater power 2,103 W yields $2{,}103 \times \frac{10}{60} \approx 350$ Wh.

2. **Takeoff transient** (≈3 min, PEM at 50% capacity): net battery demand $\approx 7{,}800\,\mathrm{W} \times \frac{3}{60} \approx 390\,\mathrm{Wh}$.

The combined baseline energy requirement is therefore ≈740 Wh. Applying a 1.30 safety and redundancy factor gives a design capacity of

$$E_{\text{bat}} = 740 \times 1.30 \approx 960\,\mathrm{Wh}. \tag{1}$$

At a cell-level specific energy of 200–250 Wh kg^{-1} (LiPo to NMC Li-ion) the pack mass is estimated at **3.8–4.8 kg**. Once the PEM is at full output the battery is trickle-charged from excess fuel-cell capacity and held at ≈80% state of charge as a contingency reserve for the remainder of the mission.

C. Heat Sources

Table 2 lists the primary waste heat sources and their locations along the hydrogen flow path, as derived from the power budget in Section 4.

Table 2: Waste heat sources and spatial distribution

Zone	URDF location	Cruise (W)	Takeoff (W)
Aft motor mount (single)	top-mounted, $x \approx -2.0\,\mathrm{m}$	221	1,000
Fuselage avionics	$x \approx -1.5\,\mathrm{m}$	80	160
PEM fuel cell stack	CoG at $x = -1.876\,\mathrm{m}$	2611	7833
Total		**2,912**	**8,993**

. LEAF-VEIN MICRO-CHANNEL SPAR ARCHITECTURE

A. Hierarchical Channel Network

Figure 1 illustrates the three-level branching architecture, which follows the same topology as a biological leaf. Each wing carries two structural spars that together form a closed H_2 circuit: a *front spar* (delivery, analogous to the leaf midrib) and a *rear spar* (return), both running spanwise and sharing the same CFRP tube cross-section ($D_o = 36\,\mathrm{mm}$, $D_i = 27\,\mathrm{mm}$). At four chordwise stations along the front wing, *secondary channels* branch orthogonally from the front spar, run chordwise to the rear spar, and are structurally equivalent to wing ribs. From each secondary, fifteen *terminal micro-channels* distribute flow spanwise across the inter-spar bay, maximising heat transfer surface area. A compact tip U-connector joins the front and rear spars at the wing tip, completing the circuit. The V-tail surfaces follow the same topology at smaller scale (two secondaries, ten terminals each).

Cryogenic hydrogen enters the wing circuit through a *dual-channel rotary union* mounted at the wing-root pivot. The union uses a concentric tube arrangement: the inner bore carries cold H_2 outbound to the front spar, while the outer annulus returns warm H_2 from the rear spar to the PEM fuel-cell bay. The bearing housing of the rotary union simultaneously transfers wing

bending and torsion loads into the fuselage, so no separate structural root fitting is required. H_2 flows spanwise along the front spar to the tip, passes through a compact U-connector into the rear spar, and returns root-ward. Because the return leg carries already-heated H_2 ($>70\,^{\circ}$C), its wall heat flux is low and does not materially alter the outlet temperature to the PEM; the thermal model in Section 4 therefore analyses the delivery leg only. Vertical metallic fin structures connect the terminal channels to the wing's inner structural sleeve, acting simultaneously as pedestal fins (extending the heat transfer surface to the wing skin) and as rib substitutes (transferring wing skin shear loads into the channel network).

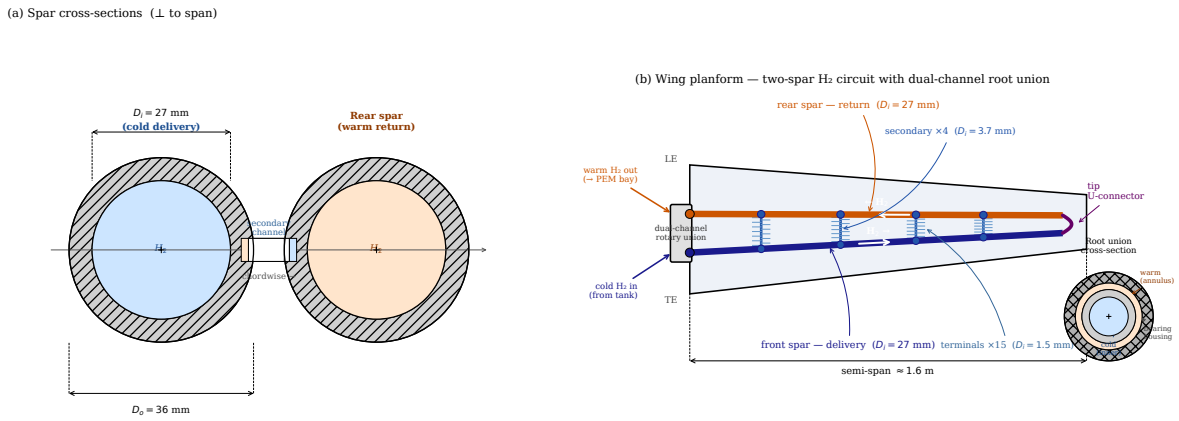

Figure 1: Leaf-vein micro-channel spar concept (two-spar closed circuit). *(a)* Cross-sections perpendicular to the span axis: front spar (cold delivery, blue) and rear spar (warm return, orange), each with CFRP outer wall ($D_o = 36\,$mm) and H_2 bore ($D_i = 27\,$mm); dashed line indicates the chordwise secondary channel connecting the two spars. *(b)* Front-wing semi-span planform of the closed H_2 circuit. A single dual-channel rotary union at the wing root (grey block, see inset) accepts cryogenic H_2 on its inner bore and returns warm H_2 through its outer annulus, with the bearing housing transferring structural wing loads into the fuselage. The front spar (blue) delivers H_2 spanwise to the tip; four chordwise secondary channels ($D_i = 3.7\,$mm) bridge the front and rear spars, each carrying fifteen spanwise terminal micro-channels ($D_i = 1.5\,$mm); the rear spar (orange) returns warm H_2 root-ward via a tip U-connector (purple) back to the rotary union outlet. *Inset:* dual-channel rotary union cross-section showing the cold inner bore, warm return annulus, and structural bearing housing. V-tail surfaces share the same topology at reduced scale ($D_i = 18\,$mm spars, $D_i = 3.2\,$mm secondaries).

B. Channel Geometry and Murray's Law Sizing

The dimensions presented below reflect the current preliminary design iteration and will be refined as structural optimisation and detailed thermal analysis mature toward a flight-ready configuration.

Channel diameters at each branching level are set by Murray's Law, which minimises total pumping power by maintaining constant wall shear stress throughout the network:

$$D_{\text{parent}}^3 = \sum_i D_{\text{child},i}^3 \tag{2}$$

The main spar diameter is governed by structural loads (Section 3.3) rather than flow requirements; the secondary and terminal diameters follow Eq. (2) upward from the chosen terminal size. Table 3 summarises the resulting geometry for both wing sets.

Table 3: Hierarchical channel network geometry

Surface	Level	Count	D_i	Sizing driver
Front wing (each)	Main spar	1	27.0 mm	Structural (bending + torsion)
	Secondary	4	3.7 mm	Murray's Law ($15^{1/3} \times 1.5$)
	Terminal	60	1.5 mm	Heat transfer / manufacturability
V-tail surface (each)	Main spar	1	18.0 mm	Structural (bending + torsion)
	Secondary	2	3.2 mm	Murray's Law ($10^{1/3} \times 1.5$)
	Terminal	20	1.5 mm	Heat transfer / manufacturability
Aircraft total — terminals		**160**	1.5 mm	120 front + 40 tail

Common parameters: wall thickness = 0.75 mm; material = Ti-6Al-4V ($k = 7\,\mathrm{W\,m^{-1}K^{-1}}$); operating pressure = 350 bar; channel wall temperature range -150 to $+100\,^{\circ}\mathrm{C}$.

C. Structural Spar Sizing

The main spar is a hollow Ti-6Al-4V shaft that rotates relative to the fuselage through cross-roller bearings and is driven by a high-torque brushless motor (harmonic drive) to provide full pitch/roll/yaw authority. It must simultaneously carry:

1. Wing root bending moment from aerodynamic lift
2. Motor torsion transmitted to the wing
3. Provide adequate shaft diameter for the motor clamp interface

At the 2.5g limit load factor, each front wing generates a root bending moment of approximately 1,575 N·m (ultimate). Combined with the 700 N·m torsion limit (URDF joint specification), the equivalent moment is:

$$M_{\text{equiv}} = \sqrt{M_b^2 + T^2} = \sqrt{1575^2 + 700^2} \approx 1{,}723\,\text{N·m} \tag{3}$$

Using Ti-6Al-4V allowable stress $\sigma_{\text{allow}} = 587\,\text{MPa}$ (yield $\div$ 1.5) and a tube wall ratio $k = D_i/D_o = 0.75$, the required outer diameter is $D_o \approx 36\,\text{mm}$, yielding $D_i \approx 27\,\text{mm}$. This spar bore is 4.6$\times$ larger than the 5.9 mm thermal-only diameter from Murray's Law, confirming that the structural requirement dominates and the H_2 flow path is readily accommodated within the structural bore with margin to spare. The V-tail spar (500 N·m limit, lower aerodynamic loads) sizes to $D_i \approx 18\,\text{mm}$ by the same procedure.

A rotary union at the wing root allows pressurised hydrogen to pass from the fixed fuselage plumbing into the rotating spar; such unions are commercially available for high-pressure applications and represent a known engineering solution for this interface.

D. Material Selection

Ti-6Al-4V is selected for the spar and channel walls on the basis of its high specific strength, good fatigue resistance under thermal cycling, and compatibility with hydrogen (no hydrogen embrittlement at the expected hydrogen partial pressures) [8]. 316L stainless steel is an alternative for the channel inserts, offering higher thermal conductivity ($k = 16\,\mathrm{W\,m^{-1}K^{-1}}$) at the cost of higher density. CFRP outer skins are bonded over the metallic spar core, providing aerodynamic surface and additional bending stiffness while maintaining radar-cross-section discipline through controlled edge alignment.

E. Electric Trim Heater

Although the wing spar absorbs significant ambient heat and captures motor waste heat, these passive sources alone are insufficient to guarantee 70–85 °C at the PEM inlet across all operational conditions. The architecture therefore includes a compact inline *electric trim heater* positioned in the fuselage section (path fraction 0.88–0.96), between the avionics zone and the PEM cooling jacket.

Operating Modes

The trim heater operates in three distinct modes:

1. **Startup (0–10 min):** The PEM stack is cold and generates no waste heat. The trim heater supplies up to 2,100 W to bring recirculating H_2 to 70 °C, enabling the fuel cell to reach self-sustaining operation. Once the PEM stack produces waste heat sufficient to maintain the inlet temperature, the trim heater throttles down.

2. **Altitude / reduced load:** At high altitude the ambient pre-heating contribution through the spar decreases (smaller ΔT between environment and cryogenic H_2), and at reduced throttle settings the PEM waste heat is proportionally lower. The trim heater compensates, maintaining outlet temperature within the 70–85 °C window. Fig. 2(d) quantifies the required power at ISA standard altitudes.

3. **Nominal steady-state cruise (primary mode):** The PEM stack generates 2,612 W of waste heat. Of this, 500 W is directly transferred to the recirculating H_2 via the compact cooling jacket; the remainder is removed by stack convection. Combined with spar pre-heating, these passive sources typically sustain the outlet temperature near target, and the trim heater operates at reduced or zero duty.

Sizing and Control

The trim heater is sized for the worst-case condition: no ambient pre-heating (e.g., ground operation in an insulated hangar or high-altitude cruise), requiring 2,103 W. In practice it is implemented as a resistance heating element wound around the H_2 supply line upstream of the PEM, with a closed-loop PID controller reading the thermocouple at the PEM inlet and modulating heater duty. At sea level cruise the nominal trim heater power is 1,220 W (47% of total electrical demand); the corresponding additional H_2 consumption during brief startup ($\sim$10 min) is negligible relative

to the 48-hour fuel budget. In steady-state operation where PEM waste heat provides the bulk of pre-heating, trim heater power is substantially reduced.

F. IR Signature Suppression

The single aft-fuselage motor mount and the PEM bay exhaust ports are the primary IR emitters on the vehicle. The motor is deliberately positioned adjacent to the LH_2 storage tank at the aft fuselage, where the cryogenic tank surface (20–120 K) and cold H_2 vapour boil-off provide a passive cold shroud around the dominant heat source. This co-location suppresses the motor mount IR plume without any additional hardware. By additionally routing the coldest hydrogen (near $-150\,^{\circ}$C) through channels adjacent to these zones, the surface temperatures of the emitting structures are further reduced. Qualitatively, the radiative power from a surface scales as T^4; reducing a motor mount from 80 °C (353 K) to 40 °C (313 K) reduces emitted power by approximately 38%. Quantitative IR signature modelling is deferred to future work integrating a Gazebo thermal plugin.

. THERMAL MODEL

A. Power Budget

Table 4 summarises the power budget for the MARID at the cruise design point. The aerodynamic drag is estimated assuming a lift-to-drag ratio of 14, representative of a clean medium-aspect-ratio fixed-wing platform at cruise.

Table 4: MARID power budget at cruise (25 m/s, $L/D = 14$)

Quantity	Value	Notes
Gross mass	113.6 kg	URDF
Aerodynamic drag	79.6 N	$W/(L/D)$
Required shaft power	1,990 W	$F_D \times V$
Motor input power (single thruster)	2,211 W	$\eta_{\text{motor}} = 0.90$; cruise sizing
Avionics + actuators	400 W	Estimate
Total electrical demand	2,611 W	
PEM chemical power input	5,222 W	$\eta_{\text{PEM}} = 0.50$
H_2 consumption (cruise)	0.044 g/s	7.52 kg per 48 hr
Motor waste heat	221 W	
PEM stack waste heat	2,611 W	
Miscellaneous waste heat	80 W	
Total cruise waste heat	**2,912 W**	
Total takeoff waste heat	**8,993 W**	single high-power motor at takeoff thrust

B. One-Dimensional Finite-Segment Formulation

The 2.25 m representative path is discretised into $N = 400$ equal segments of length $\Delta x = L/N = 5.625$ mm. At each segment i, the fluid temperature T_i is updated by:

$$T_{i+1} = T_i + \frac{\dot{q}_i \, \Delta x}{\dot{m}_{\text{total}} \, c_p(T_i)} \tag{4}$$

where $\dot{q}_i$ (W m^{-1}) is the distributed heat flux at position x_i/L and $c_p(T_i)$ is the temperature-dependent specific heat of gaseous hydrogen. The channel wall temperature is:

$$T_{\text{wall},i} = T_i + \frac{\dot{q}_i}{h_i \, \pi D_i} \tag{5}$$

where h_i is the convective heat transfer coefficient derived from the Nusselt number correlation appropriate to the local flow regime.

C. Hydrogen Thermophysical Properties

Thermophysical properties of gaseous hydrogen at 350 bar are approximated by polynomial fits to NIST WebBook data over the range 100–420 K:

$$c_p(T) = 12{,}200 + 8.0(T - 100) - 0.012(T - 100)^2 \quad [\text{J kg}^{-1}\text{K}^{-1}] \tag{6}$$

$$k(T) = 0.065 + 5.83 \times 10^{-4}(T - 100) \quad [\text{W m}^{-1}\text{K}^{-1}] \tag{7}$$

$$\mu(T) = [4.2 + 0.0163(T - 100)] \times 10^{-6} \quad [\text{Pa s}] \tag{8}$$

The mean specific heat over the operating range (123–353 K) is approximately 13,500 J kg^{-1}K^{-1}—nearly 3.2$\times$ that of water and 6.8$\times$ that of thermal oil.

D. Nusselt Number Correlation

The Reynolds number per channel is:

$$Re = \frac{4 \, \dot{m}_{\text{ch}}}{\pi D_i \mu} \tag{9}$$

For $Re < 2{,}300$ (laminar), uniform-heat-flux internal pipe flow: $Nu = 4.36$. In the transition region ($2{,}300 < Re < 10{,}000$), the Gnielinski correlation is applied [9]. For fully turbulent flow ($Re > 10{,}000$), Dittus-Boelter is used: $Nu = 0.023 \, Re^{0.8} \, Pr^{0.4}$.

E. Results

4.5.1 Flow Regime

At the design cruise flow rate of 0.984 g/s distributed across 160 terminal channels, the per-channel mass flow is 6.15 mg/s. At a mean temperature of 220 K the dynamic viscosity is $\mu \approx 6.2 \times 10^{-6}$ Pa s, yielding:

$$Re = \frac{4 \times 6.15 \times 10^{-6}}{\pi \times 1.5 \times 10^{-3} \times 6.2 \times 10^{-6}} \approx 840 \tag{10}$$

The flow is *laminar* throughout the operating range ($Re < 2{,}300$), confirming constant $Nu = 4.36$ and negligible pressure drop (Section 6). This is significant for two reasons: (i) the Nusselt number

is constant ($Nu = 4.36$), simplifying design analysis; and (ii) the pressure drop is minimised, reducing the recirculation pump power requirement to negligible levels (Section 6).

4.5.2 Temperature Profiles and Ambient Pre-Heating

Figure 2(a) shows the H_2 temperature profile along the corrected 2.25 m series path (1.50 m main spar + 0.40 m chordwise secondaries + 0.15 m terminals + 0.20 m fuselage) for three cases at the fixed design flow rate of 0.984 g/s (23:1 recirculation).

The dash-dot grey curve (internal heat sources only, no ambient, no trim heater) reveals the thermal path structure: a small temperature rise at 0–0.23 m (motor mounts, 221 W), a nearly flat plateau from 0.23 to 2.07 m (no internal sources), and a moderate step at 2.16 m where the PEM cooling jacket delivers 500 W to the H_2 in the final 4% of path. Without ambient or trim heating the outlet reaches only $-84.7\,^{\circ}$C—far below the 70–85 °C target. The PEM cooling jacket alone cannot close the energy balance, because PEM operation itself requires pre-heated H_2 at the inlet.

The solid blue curve adds ambient pre-heating through the titanium spar wall. Cryogenic hydrogen at $-150\,^{\circ}$C is separated from ambient air at $+15\,^{\circ}$C (sea level ISA) only by the spar wall; the initial temperature differential is 165 K. The convective-conductive conductance per unit length is $UA_{\text{spar}} \approx 4.6\,\text{W}\,(\text{m K})^{-1}$, and the 1.5 m spar absorbs approximately 883 W—replacing the flat plateau with a continuous rise. At 0.984 g/s the outlet reaches only $-15.6\,^{\circ}$C: ambient pre-heating alone is insufficient.

The heavy blue curve adds the electric trim heater (Section 3.5) at 1,220 W (sea level). H_2 exits at 77.3 °C—within the 70–85 °C PEM operating window. The red shaded region in Figure 2(a) marks the trim heater zone (path fraction 0.88–0.96).

4.5.3 Outlet Temperature vs. Flow Rate — Altitude Parametric

Figure 2(b) shows outlet temperature as a function of total flow rate for five ISA conditions: sea level ($+15\,^{\circ}$C), 2,000 m ($+2\,^{\circ}$C), 5,000 m ($-17.5\,^{\circ}$C), tropopause ($-56.5\,^{\circ}$C), and the no-ambient worst case. No trim heater is applied in these sweeps. The green band marks the 70–85 °C target. At no flow rate does any altitude curve reach the target band without the trim heater, confirming that ambient pre-heating alone is insufficient and the trim heater is structurally necessary at all altitudes. The flow rate is fixed at 0.984 g/s (23:1 recirculation); the trim heater compensates rather than adjusting flow (Figure 2d).

4.5.4 Maximum Wall Temperature

The peak channel wall temperature at the terminal micro-channel exits (PEM bay, end of path) is estimated at approximately 100 °C for the internal-only baseline—well below the yield temperature of Ti-6Al-4V (>900 °C) and below the CFRP epoxy ceiling (≈150 °C). Along the main spar, although the cryogenic H_2 enters at $-150\,^{\circ}$C, the large bore ($D_i = 27$ mm) and moderate UA ensure that the spar wall temperature remains between the ambient and fluid temperatures throughout. The spar cross-section is structurally safe across the full thermal duty cycle.

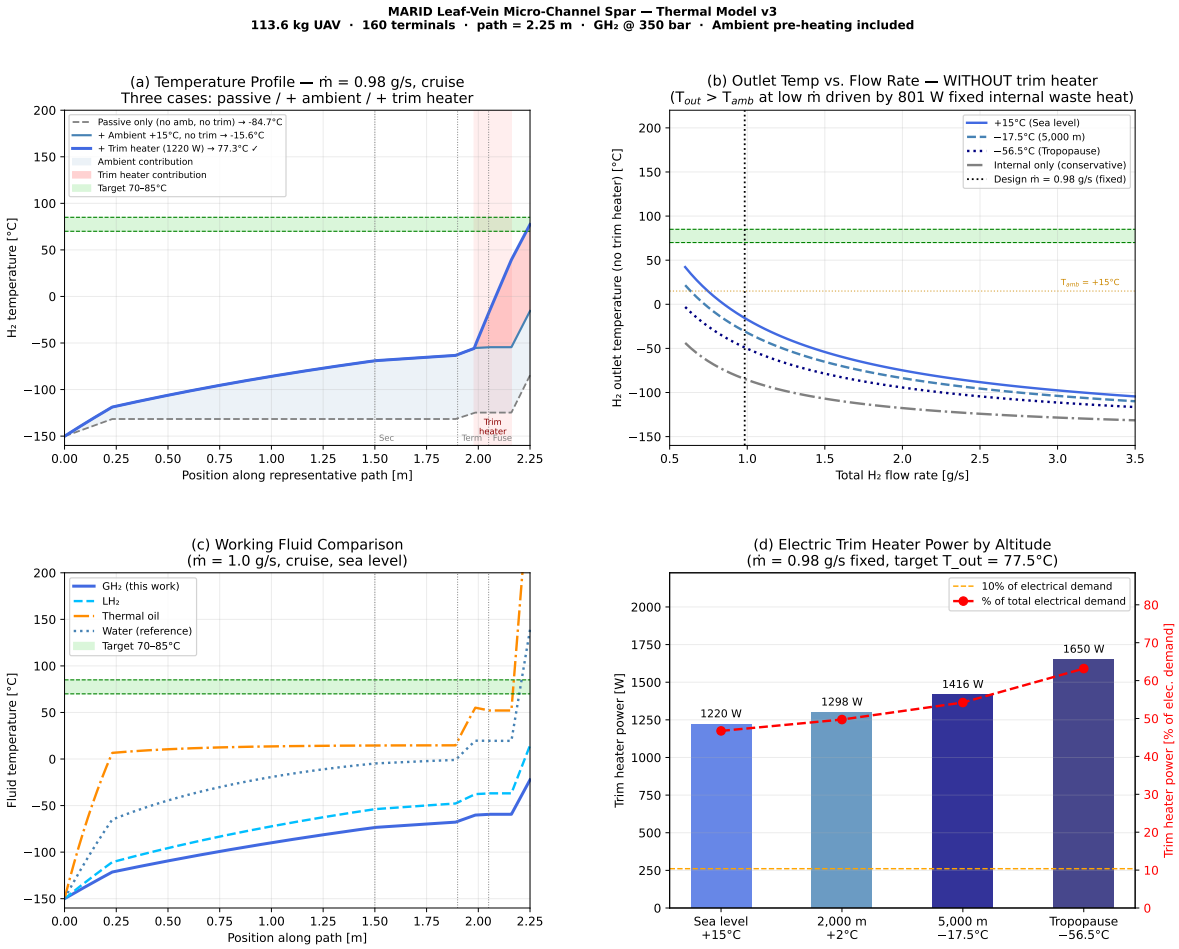

Figure 2: Thermal model results (v4 model, 160 terminals, 2.25 m path, fixed design flow 0.984 g/s, 23:1 recirculation). (a) H_2 temperature profile along the series path for three cases: dash-dot grey = internal sources only (exits $-84.7\,^{\circ}$C); solid blue = +sea-level ambient pre-heating only (exits $-15.6\,^{\circ}$C); heavy blue = +electric trim heater 1,220 W (exits 77.3 °C ✓); red fill = trim heater contribution; blue fill = ambient contribution; red shading = trim heater zone (0.88–0.96 path fraction); green band = 70–85 °C PEM operating window. (b) Outlet temperature vs. total flow rate for five altitude conditions (no trim heater); no curve reaches the target band, confirming the trim heater is structurally necessary at all altitudes. (c) Working fluid comparison at 1.0 g/s, sea level. (d) Required trim heater power by ISA altitude (bars) and fraction of total electrical demand (red line); sea level 1,220 W (46.7%), tropopause 1,650 W (63.2%).

. WORKING FLUID TRADE STUDY

Figure 2(c) compares four candidate working fluids at a common total flow rate of 1.0 g/s under cruise heat loading. Table 5 summarises their properties.

Gaseous hydrogen's specific heat is $3.2\times$ that of thermal oil and $6.8\times$ that of water, making it uniquely suited to absorb the large enthalpy required to heat from $-150\,^{\circ}$C to $+80\,^{\circ}$C. Critically, GH_2 is the fuel itself—no additional working fluid, pump, or reservoir is required; the recirculation pump circulates fuel that is being consumed anyway.

Table 5: Working fluid comparison at mean operating temperature

Fluid	c_p (J kg^{-1}K^{-1})	$\Delta T_{\max}$ at 1 g/s	Notes
GH_2 (this work)	13,500	216 K	Fuel = coolant; no added mass
LH_2	9,700	300 K	Phase change adds complexity
Thermal oil	2,000	1,456 K†	Exceeds structural limits
Water (ref.)	4,186	696 K†	Freezes; not suitable

† Outlet temperature would exceed 1,000 °C, indicating the fluid cannot absorb the waste heat at this flow rate without vaporisation or structural failure. A much higher flow rate would be required, imposing a dedicated pump mass.

Liquid hydrogen offers a higher ΔT capacity but introduces phase-change physics (boiling onset at -253 °C at 1 bar), complex insulation requirements, and potential two-phase flow instability in micro-channels. The present analysis recommends GH_2 for initial prototype development, with LH_2 as a follow-on option once single-phase GH_2 behaviour is validated.

. RECIRCULATION PUMP ANALYSIS

A. Required Flow Rate vs. Fuel Consumption

At cruise, the fuel cell consumes hydrogen at $\dot{m}_{\text{fuel}} = 0.044$ g/s. The thermal management system operates at a fixed total channel flow of 0.984 g/s, giving a *recirculation ratio* of 23:1. The flow rate is held constant across altitudes; the electric trim heater (Section 3.5) adjusts its power output to maintain the 70–85 °C PEM inlet temperature rather than varying the flow rate. A fixed flow rate simplifies the recirculation pump design and avoids transient hydraulic effects during altitude transitions.

The fuel supply system must incorporate a recirculation pump that circulates 23 volumes of hydrogen for every volume consumed by the fuel cell. The surplus hydrogen is recirculated to the cryo storage vessel or through a bypass loop.

B. Pump Power

In a Murray's Law branching network, the total pressure drop from root to terminal is the sum of the drops across each level. For laminar flow at each level, Hagen-Poiseuille applies:

$$\Delta P_{\text{level}} = \frac{128\,\mu\,L_{\text{level}}\,\dot{Q}_{\text{branch}}}{\pi\,D_{i,\text{level}}^4} \tag{11}$$

where $\dot{Q}_{\text{branch}}$ is the volumetric flow in one branch at that level. At 350 bar and 200 K, GH_2 density $\rho \approx 30\,\text{kg m}^{-3}$ and $\mu \approx 6.2 \times 10^{-6}$ Pa s.

For the front wing network at the conservative baseline flow $\dot{m} = 0.984$ g/s:

$$\dot{Q}_{\text{main}} = \frac{0.984 \times 10^{-3}}{30} = 3.28 \times 10^{-5}\ \text{m}^3\text{s}^{-1} \quad (D_i = 27\,\text{mm},\ L \approx 0.5\,\text{m}) \tag{12}$$

$$\dot{Q}_{\text{secondary}} = \dot{Q}_{\text{main}}/4 = 8.2 \times 10^{-6}\ \text{m}^3\text{s}^{-1} \quad (D_i = 3.7\,\text{mm},\ L \approx 0.4\,\text{m}) \tag{13}$$

$$\dot{Q}_{\text{terminal}} = \dot{Q}_{\text{secondary}}/15 = 5.5 \times 10^{-7}\ \text{m}^3\text{s}^{-1} \quad (D_i = 1.5\,\text{mm},\ L \approx 0.15\,\text{m}) \tag{14}$$

Summing Hagen-Poiseuille drops across all three levels:

$$\Delta P_{\text{main}} \approx 0.4\ \text{Pa} \qquad (27\,\text{mm bore, high flow, low resistance}) \tag{15}$$

$$\Delta P_{\text{secondary}} \approx 7.0\ \text{Pa} \tag{16}$$

$$\Delta P_{\text{terminal}} \approx 20\ \text{Pa} \qquad (\text{dominant level}) \tag{17}$$

$$\Delta P_{\text{total}} \approx 27\ \text{Pa} \tag{18}$$

The main spar contributes negligibly due to its large bore ($D_i = 27\,\text{mm}$); the terminal channels dominate—consistent with biological vascular systems where capillary resistance is the largest single contributor to total pressure drop.

The total pump power for 160 terminal channels at 60% pump efficiency is:

$$P_{\text{pump}} = \frac{\Delta P_{\text{total}} \times \dot{Q}_{\text{total}}}{\eta_{\text{pump}}} = \frac{27 \times 3.28 \times 10^{-5}}{0.6} \approx 0.0015\,\text{W} \tag{19}$$

The pump adds less than 0.01% of the total electrical demand—an entirely negligible parasitic load. The large main spar bore ($D_i = 27\,\text{mm}$) ensures that network resistance is dominated by the fine terminal channels, exactly as in biological vascular systems. The recirculation pump can be implemented as a miniature cryogenic centrifugal or peristaltic pump with trivial mass and power budget.

C. Implications for 48-Hour Endurance

The 48-hour design endurance requires 7.52 kg of H_2 at the computed fuel-cell consumption rate (Table 4). The recirculation pump itself adds no hydrogen mass consumption. The electric trim heater draws electrical power from the fuel cell rather than consuming additional H_2 directly; however, increased electrical demand reduces overall fuel cell efficiency.

In the *nominal cruise* operating mode the trim heater is at reduced or zero output: the PEM stack, once at operating temperature, delivers waste heat beyond the modelled 500 W floor and naturally supplements the H_2 pre-heating. The endurance penalty in this mode is negligible.

If the trim heater were operated continuously at the sea-level nominal power of 1,220 W, the additional H_2 consumption would be approximately $1{,}220/(0.5 \times 120 \times 10^6) \approx 0.020$ g/s, adding ≈3.5 kg of H_2 over 48 hours—a 47% increase in the H_2 budget. The trim heater is therefore operated as a *startup and contingency* element only:

- **Startup** (0–10 min): full power ($\lesssim$2,100 W) to bring H_2 to 70 °C before fuel cell ignition.
- **Altitude excursions / reduced PEM load**: variable supplement when PEM waste heat is insufficient.

- **Nominal cruise**: reduced or zero output; PEM waste heat sustains the target temperature.

Under this operating profile the 48-hour H_2 budget remains close to 7.52 kg, with any trim-heater contribution limited to the transient start-up period.

Whether the airframe can accommodate 7.52 kg of compressed hydrogen within the structural and volumetric budget is a separate system-level trade (GH_2 at 350 bar requires $\approx$313 L; LH_2 at 70 kg m^{-3} requires $\approx$107 L) and is outside the scope of this paper. The thermal architecture presented here is compatible with either storage approach.

. DISCUSSION

A. Mass Savings

A conventional thermal management system for a UAV of this class would require: (i) a H_2 pre-heater heat exchanger, estimated at 0.5–2 kg for the required 2,912 W duty; (ii) a coolant pump and reservoir for PEM cooling, estimated at 1–3 kg; and (iii) associated plumbing, fittings, and insulation. The leaf-vein spar architecture eliminates all three subsystems, with the only addition being the recirculation pump (< 0.1 kg). The net mass saving is estimated at 2–5 kg, translating directly to additional H_2 carrying capacity and increased endurance.

B. Manufacturing Considerations

Embedding 160 terminal channels of 1.5 mm diameter in titanium spars is achievable by two established processes: (i) *electron beam melting (EBM)* additive manufacturing, which can produce complex internal channel networks in Ti-6Al-4V directly from CAD; and (ii) *diffusion bonding* of photo-chemically etched titanium foils, a mature process used in compact heat exchangers for aerospace applications. Channel tolerances of ± 0.05 mm are achievable with both methods [10, 11].

C. Laminar Flow Regime

The operating Reynolds number ($Re \approx 840$) places the flow firmly in the laminar regime throughout the operating range. This has two design consequences. First, the heat transfer coefficient is lower than turbulent flow would provide, but the large number of channels and the high specific heat of GH_2 more than compensate—as demonstrated by the thermal model closure. Second, the pressure drop is minimised, enabling the negligibly small pump power computed in Section 6. Should future designs require higher heat flux (e.g., larger PEM stacks), transitioning to turbulent flow by reducing channel diameter or increasing flow rate is straightforward.

D. Limitations and Future Work

The present analysis makes several simplifying assumptions that will be addressed in future work:

- **1-D model**: Radial temperature gradients within the spar cross-section and circumferential conduction between channels are neglected. A full 3-D conjugate heat transfer model (e.g., in OpenFOAM or ANSYS Fluent) will be developed.

- **Constant heat loads**: Heat loads are assumed steady at the cruise and takeoff values. A transient model capturing the thermal time constants of the spar and fuel cell will be needed for control system design.
- **Structural analysis**: A detailed FEA of the spar cross-section with 160 channel voids under combined bending, torsion, and thermal loading is in progress.
- **Gazebo thermal simulation**: A lumped-parameter ROS2 node coupled to a Gazebo system plugin will simulate in-flight temperature evolution and IR signature maps, enabling real-time thermal management in the flight stack.
- **GH_2 vs LH_2 transition**: Phase-change effects for liquid hydrogen storage will be incorporated in a follow-on study.
- **Incomplete mass budget**: The 113.6 kg gross mass used throughout is the URDF structural baseline and understates the real MTOW. Missing contributions include the single high-power thruster system (motor + propeller + ESC, 7–16 kg), LH_2 fuel and cryogenic tank (43–53 kg), the 960 Wh startup and contingency battery pack (3.8–4.8 kg at 1.30× safety factor), PEM stack, and sensor payload, yielding an estimated real MTOW of **175–210 kg**. Power and drag figures scale proportionally; a full mass-budget closure is left for the system-level design study.
- **Motor heat-source location**: The thermal model currently deposits motor waste heat at the start of the series path (wing root region). With the single aft-fuselage motor, this heat source moves to the fuselage segment ($x \approx 2.0$ m along the 2.25 m path). Updated 1-D and 3-D models reflecting this geometry will be presented in future work.

. CONCLUSION

A leaf-vein micro-channel spar architecture has been proposed and analysed for the MARID hydrogen fuel-cell UAV (113.6 kg structural baseline; estimated real MTOW 175–210 kg). The architecture embeds 160 terminal micro-channels ($D_i = 1.5$ mm) within the primary wing and V-tail spars across a corrected 2.25 m series path, allowing cryogenic hydrogen to serve simultaneously as the propellant and the thermal management working fluid.

The one-dimensional thermal model demonstrates:

1. **Trim heater closes the energy balance**: At the fixed design flow of 0.984 g/s (23:1 recirculation), internal waste heat alone yields $-84.7\,^{\circ}$C at the outlet; adding sea-level ambient pre-heating raises this to only $-15.6\,^{\circ}$C. An electric trim heater of 1,220 W (sea level) to 1,650 W (tropopause) brings the outlet to 77.3 °C, within the 70–85 °C PEM operating window at all altitudes.
2. **Ambient pre-heating supplements but cannot substitute**: The 1.5 m cryogenic spar absorbs ≈883 W from ambient air at sea level, representing a significant free energy input. However, internal waste heat and ambient contribution together fall short of the target by more than 90 °C at sea level, confirming that the trim heater is structurally necessary rather than optional.

3. **Negligible pump overhead**: The fixed 23:1 recirculation ratio requires only 0.0015 W of pump power ($<0.01\%$ of total electrical demand). The large main spar bore (27 mm front, 18 mm tail) ensures terminal channels dominate network resistance, as in biological vascular systems.

4. **Structural spar**: The main spar diameter is governed by combined bending and torsion loads ($D_o \approx 36$ mm, $D_i \approx 27$ mm front), which is 4.6$\times$ the thermally-required bore—structural and thermal functions are fully compatible.

5. **Fluid selection**: GH_2's specific heat ($\approx$13,500 J kg^{-1}K^{-1}) is uniquely suited; thermal oil and water require flow rates incompatible with the channel geometry.

6. **Mass savings**: Elimination of dedicated pre-heater and cooling subsystems reduces dry mass by an estimated 2–5 kg, directly improving endurance.

7. **Startup/contingency trim heater architecture**: Operating the trim heater continuously at sea-level power (1,220 W) would increase the 48-hour H_2 budget by $\approx$47%. The architecture avoids this penalty by using the trim heater as a startup device (0–10 min, $\lesssim$2,100 W to initialise the PEM) and an altitude contingency supplement, with nominal cruise sustained by PEM waste heat alone. The endurance impact is therefore limited to the transient start-up period.

Future work will extend the analysis to full 3-D conjugate heat transfer, structural FEA with channel voids, transient thermal modelling, and integration with the Gazebo-based flight simulation environment.

ACKNOWLEDGEMENTS

The author thanks the open-source ROS2, Gazebo, and FAST-LIO communities whose tools underpin the simulation environment used in this work.

NOMENCLATURE

c_p	specific heat at constant pressure, J kg^{-1}K^{-1}
D_i	channel inner diameter, m
h	convective heat transfer coefficient, W m^{-2}K^{-1}
k	thermal conductivity, W m^{-1}K^{-1}
L	channel path length, m
$\dot{m}$	mass flow rate, kg s^{-1}
N_{ch}	number of micro-channels
Nu	Nusselt number
ΔP	pressure drop, Pa
$\dot{Q}$	volumetric flow rate, m^3 s^{-1}
$\dot{q}$	heat flux per unit length, W m^{-1}
Re	Reynolds number
T	temperature, K or °C (stated in context)
μ	dynamic viscosity, Pa s
η	efficiency
Subscripts	
ch	per channel
fuel	hydrogen fuel consumption
thermal	thermal management circuit
wall	channel wall surface

References

[1] Bradley, T. H., Moffitt, B. A., Parekh, D. E., and Mavris, D., "Development and Experimental Characterization of a Fuel Cell Powered Aircraft," *Journal of Power Sources*, Vol. 171, No. 2, 2007, pp. 793–801.

[2] Larminie, J., and Dicks, A., *Fuel Cell Systems Explained*, 2nd ed., Wiley, Chichester, UK, 2003.

[3] Gong, A., and Verstraete, D., "Fuel Cell Propulsion in Small Fixed-Wing Unmanned Aerial Vehicles: Current Status and Research Needs," *International Journal of Hydrogen Energy*, Vol. 42, No. 33, 2017, pp. 21311–21333.

[4] Katifori, E., Szöllősi, G. J., and Magnasco, M. O., "Damage and Fluctuations Induce Loops in Optimal Transport Networks," *Physical Review Letters*, Vol. 104, 2010, 048704.

[5] Silverman, E. M., Griese, R. W., and Frei, W., "Using Multifunctional Structure to Reduce Spacecraft Cost," *Acta Astronautica*, Vol. 52, Nos. 9–12, 2003, pp. 785–791.

[6] Heenan, T. M. M., et al., "An Advanced Microstructural and Electrochemical Datasheet on 18650 Li-Ion Batteries with Nickel-Rich NMC811 Cathodes and Graphite-Silicon Anodes," *Journal of the Electrochemical Society*, Vol. 167, 2020, 140530.

[7] Thomas, J. P., and Qidwai, M. A., "The Design and Application of Multifunctional Structure-Battery Materials Systems," *JOM*, Vol. 57, No. 3, 2005, pp. 18–24.

[8] San Marchi, C., and Somerday, B. P., *Technical Reference for Hydrogen Compatibility of Materials*, Sandia National Laboratories, SAND2012-7321, 2012.

[9] Gnielinski, V., "New Equations for Heat and Mass Transfer in Turbulent Pipe and Channel Flow," *International Chemical Engineering*, Vol. 16, No. 2, 1976, pp. 359–368.

[10] Murr, L. E., et al., "Metal Fabrication by Additive Manufacturing Using Laser and Electron Beam Melting Technologies," *Journal of Materials Science & Technology*, Vol. 28, No. 1, 2012, pp. 1–14.

[11] Martindale, B., and Bhave, R., "Perforated Plate Support for Micro-Channel Heat Exchangers," in *Compact Heat Exchangers for the Process Industries*, Begell House, 1997.

[12] Chalak, M., "Multi-Axis Rotary-Wing Integrated Drone (MARID)," *MChalak Aerospace Blog*, July 2024, `https://mchalakaerospace.blogspot.com/2024/07/multi-axis-rotary-wing-integrated.html` [retrieved April 2026]; source code and simulation model available at `https://github.com/MChalak1/MARID_UAV` [retrieved April 2026].